

OBSERVATIONS OF SEVERE LOCAL STORMS AND TORNADOES WITH THE ATMOSPHERIC IMAGING RADAR

JAMES M. KURDZO, FENG NAI, DAVID J. BODINE, TIMOTHY A. BONIN, ROBERT D. PALMER,
BOON LENG CHEONG, JAVIER LUJAN, ANDREW MAHRE, AND ANDREW D. BYRD

Radar imaging data of severe local storms and tornadoes are presented at high spatial and temporal resolutions.

The observation of severe local storms and tornadoes is limited by their relatively short lifespans, small scales, and rapid evolution. Radar has contributed a significant amount of detail to our current understanding of these phenomena (Markowski and Richardson 2014), but the limitations of radar include its often fixed location (e.g., Crum and Alberty 1993) and relatively slow rate of scanning (Brown et al. 2005;

Heinselman et al. 2008). Mobile radars developed for the purpose of observing convective storms at close range have become more common (e.g., Wurman et al. 1996; Bluestein and Pazmany 2000; Wurman and Gill 2000), leading to higher spatial resolutions and the ability to observe storm dynamics at low elevations (Wurman 2002; Bluestein et al. 2007a; Wurman and Kosiba 2013). Overall, numerous studies have utilized mobile radar for multiple-Doppler analysis of supercells and tornadoes (e.g., Wurman et al. 2007a,b; Marquis et al. 2008; Wurman et al. 2010; Kosiba et al. 2013); polarimetric observations of convective storms (e.g., Frame et al. 2009; Tanamachi et al. 2012; Snyder et al. 2013; French et al. 2015a; Houser et al. 2016); and volumetric scanning for analysis of tornadogenesis, tornadic dissipation and structure, and tornado damage (e.g., Wurman and Alexander 2005; French et al. 2013; Snyder and Bluestein 2014; Houser et al. 2015).

With many tornadoes occurring on time scales on the order of 10 s or less (e.g., Wurman and Randall 2001; Wurman 2002; Wurman et al. 2007a; Bluestein et al. 2010; French et al. 2014; Wurman et al. 2013, 2014; Snyder and Bluestein 2014), only the most rapidly scanning, high-resolution mobile radars can sufficiently capture the full evolution of some tornadoes

AFFILIATIONS: KURDZO,* NAI, PALMER, CHEONG, LUJAN, MAHRE, AND BYRD—Advanced Radar Research Center, University of Oklahoma, Norman, Oklahoma; BODINE—Advanced Study Program, NCAR, Boulder, Colorado; BONIN—Cooperative Institute for Research in Environmental Sciences, Boulder, Colorado

***CURRENT AFFILIATION:** KURDZO—MIT Lincoln Laboratory, Lexington, Massachusetts

CORRESPONDING AUTHOR: James M. Kurdzo,
james.kurdzo@ll.mit.edu

The abstract for this article can be found in this issue, following the table of contents.

DOI:10.1175/BAMS-D-15-00266.1

A supplement to this article is available online (10.1175/BAMS-D-15-00266.2)

In final form 28 July 2016

©2017 American Meteorological Society

(e.g., Bluestein et al. 2003, 2014). There are four existing mobile platforms that fit this description: the Rapid-Scan Doppler on Wheels (RSDOW; Wurman and Randall 2001), the Mobile Weather Radar 2005 X-Band Phased Array (MWR-05XP; Bluestein et al. 2010), the rapid X-band polarimetric radar (RaXPoI; Pazmany et al. 2013), and the Atmospheric Imaging Radar (AIR; Isom et al. 2013). These systems have combined to offer an impressive subset of severe local storm and tornado studies that push the boundaries of temporal resolution while maintaining volumetric scanning capabilities (French et al. 2014; Kosiba and Wurman 2013; Wurman et al. 2013, 2014; French et al. 2015b; Houser et al. 2015; Wakimoto et al. 2015, 2016).

The four current rapid-scanning mobile weather radars incorporate different engineering techniques to achieve their missions, with different trade-offs leading to areas of focus and drawbacks for each system. RaXPoI, the only dish-based platform in the group, makes use of a 180° s^{-1} pedestal rotation rate and frequency hopping to maintain a sufficient number of independent samples while also collecting polarimetric data in a full volume (360°). MWR-05XP utilizes a single pencil beam that is steered electronically across the face of a planar array, resulting in the ability to rapidly steer the beam across either a sector volume (less than 360°) or a full volume. RSDOW scans a full volume by leveraging a slotted waveguide array that can form separate pencil beams at multiple elevations simultaneously by using

different frequencies for each beam. Finally, the AIR scans sector volumes using a wide vertical fan beam on transmit and digital beamforming on receive to create 20 pencil beams with each pulse. RaXPoI can complete a full 20° vertical volume in approximately 40–50 s (or fewer elevations in less time), MWR-05XP can obtain 7-s sector volumes with a 2.0° effective beamwidth, RSDOW achieves 7-s (14 s) full volumes with 6 (12) pencil beams (0.9° in width), and the AIR completes a $90^\circ \times 20^\circ$ sector volume in under 6 s. Each system operates at X band (roughly 3-cm wavelength), and they are summarized in Table 1.

The purpose of this paper is to highlight data collected between 2013 and 2015 by the AIR and discuss the evolution of features seen on time scales of 10 s or less. This paper discusses what the AIR can bring to the current mobile radar landscape and how it can contribute to observations made by current rapid-scanning radars. While each radar has its own advantages and disadvantages, it is important to note that, as described in Isom et al. (2013), the AIR achieves the goal of rapid scanning in a different fashion than the other systems, leading to new benefits, but also new challenges. These trade-offs and the radar design are discussed in the next section, and improvements to the AIR since Isom et al. (2013) are detailed, including operating modes and descriptions of field campaign strategies. This review is followed by a series of example cases presented for analysis. A brief summary of how the AIR contributes to current rapid-scanning mobile radar

TABLE 1. Comparison of rapid-scan radars.

	AIR^a	RaXPoI^b	MWR-05XP^c	Rapid-DOW^d
Frequency	X band	X band	X band	X band
Transmitter	3.5 kW TWT	20 kW TWT	16 kW TWT	40 kW TWT
Polarization	Single (H)	Dual (H/V)	Single (H)	Single (H)
Beamwidth azim.	1.0°	1.0°	1.8°	0.9°
Beamwidth elev.	1.0°	1.0°	1.9°	0.9°
Vertical beam spacing	1.0°	1.0°	1.9°	Variable
Sensitivity at 10 km	12 dBZ	−7 dBZ	−15 dBZ	10 dBZ
Range resolution	37.5 m	30 m	150 m	11 m
Antenna type	Phased array	Parabolic dish	Phased array	Phased array
Scan method ^e	Imaging	Spotlight (M)	Spotlight (E)	Spotlight (M/E)
$90^\circ \times 20^\circ$ scan time	5.5 s	N/A	7 s	N/A
$360^\circ \times 20^\circ$ scan time	N/A	40 s	24 s	7/14 s

^a From Isom et al. (2013). Addition of pulse compression from this study is assumed for sensitivity and range resolution.

^b From Pazmany et al. (2013). High-resolution (30 m) mode is assumed for sensitivity.

^c From Bluestein et al. (2010).

^d From Wurman and Randall (2001) and J. Wurman (2016, personal communication). Scan times represent one/two 6-beam modes, changing vertical beam spacing.

^e M = mechanical, E = electronic.

capabilities and what the future holds for atmospheric imaging is presented at the end of this paper.

THE ATMOSPHERIC IMAGING RADAR. The AIR (shown in Fig. 1a) was first described in Isom et al. (2013), where more details on system specifics and design can be found. The AIR operates at X band and utilizes a technique known as digital beamforming, or radar imaging (Mead et al. 1998), which can be compared to the wide transmitted flash of a camera that is formed into pixels by the sensor (or receiver). Before the AIR, atmospheric imaging had only been used in the wind profiling community (Mead et al. 1998; Palmer et al. 2005; Cheong et al. 2008), although this method has since been adapted on other volumetric weather radars (Ushio et al. 2014; Adachi et al. 2016; Otsuka et al. 2016). An antenna is used to transmit a horizontally polarized vertical fan beam that is 20° in elevation and 1° in azimuth. Instead of receiving with the same antenna, a 36-element array is used to collect 36 simultaneous channels of receive data. These channels are combined using digital beamforming to create twenty $1^\circ \times 1^\circ$ beams, resulting in a simultaneous range–height indicator (RHI) with every pulse (Fig. 1b). It is important to note that despite being capable of displaying data in the traditional sense of an RHI, the AIR does not scan vertically in elevation; therefore, a more appropriate designation may be a “pseudo” RHI. However, given that the analysis capabilities and display mechanisms are essentially the same as a traditional RHI-scanning radar, the term RHI is used throughout the remainder of the paper with the acknowledgment of its differences from the traditional definition.

Since all of the data from these elevations are collected simultaneously, the antennas only have to be mechanically steered in azimuth, not in elevation (similar to MWR-05XP and RSDOW). By only collecting data in azimuthal sectors toward the rear of the vehicle, a

pedestal rotation rate of 20° s^{-1} allows the AIR to complete a $90^\circ \times 20^\circ$ sector volume in under 6 s. A listing of AIR system characteristics is provided in Table 2. The imaging technique allows for a continuous set of 1° beams in elevation, meaning that traditional RHI data can be analyzed at any azimuth in postprocessing (similar to RSDOW). The AIR provides continuous spacing of 1° , allowing for RHIs at full resolution without any interpolation. The AIR is well suited for observations of meteorological phenomena that evolve quickly and are finescale in nature. At a range of 5 km, a native volume cell would be $88 \text{ m} \times 88 \text{ m} \times 37.5 \text{ m}$ (in azimuth, elevation, and range, respectively) and is typically oversampled by a factor of 2 in azimuth and

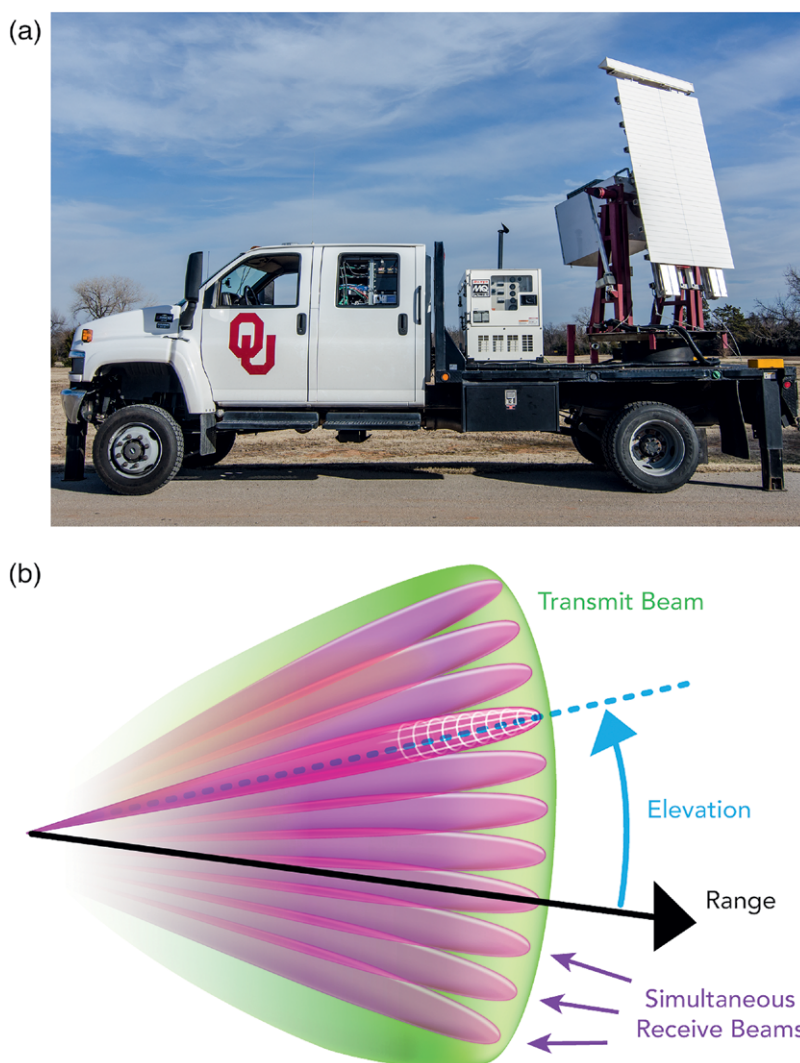


FIG. 1. (a) The AIR. The receive array is mounted on a pedestal on the bed of the vehicle, with the transmit feed horn above the array and the traveling wave tube (TWT) transmitter in the box behind the array. **(b) Concept of imaging** using a wide transmit beam (green) via a feed horn and narrow receive beams (purple) via digital beamforming using the receive array of 36 elements.

elevation, and to 30 m in range. In typical scanning scenarios, an average update rate is 6.5 s, covering approximately 110° in azimuth and 20° in elevation.

Field campaign strategies and alterations. The AIR has been modified from its form described in Isom et al. (2013) to be better suited for severe convective storm field operations. The first AIR field campaign took place in the spring of 2012 with a preliminary 1- μ s pulse and no frequency modulation, resulting in low sensitivity and limited range resolution (150 m). Additionally, an experimental staggered pulse repetition time (PRT) strategy was utilized to assist with velocity unfolding. Because of technical difficulties with the radar, no radial velocity (v_r) estimates prior to 2014 are presented in this paper. In 2013, pulse

compression was implemented on the AIR in order to mitigate the sensitivity issues and increase native range resolution. Based on the staggered PRT strategy and duty cycle limitations, a pulse length of 9 μ s was chosen for maximum sensitivity. This provided a 9.3-dB improvement over the original 1- μ s/150-m pulse, and with a 5-MHz frequency “chirp,” yielded a 45-m native range resolution (Kurdzo et al. 2014). In 2014 and 2015, a final operational pulse length of 5.25 μ s was chosen, along with a single PRT of 314 μ s. This resulted in a native range resolution of 37.5 m and a Nyquist velocity of 25 m s⁻¹. The field campaign strategies between 2012 and 2015 are summarized in Table 2.

Trade-offs of rapid-scan radars. The technique of atmospheric imaging brings advantages and disadvantages

TABLE 2. AIR system characteristics and field campaigns.

System characteristics	
Transmitter type	Traveling wave tube
Peak power	3.5 kW
Operating frequency	9,550 MHz
Sensitivity	12 dBZ @ 10 km
Observable range	40 km
Polarization	Horizontal
Transmit beamwidth (elevation dimension)	20.0°
Transmit beamwidth (azimuth dimension)	1.0°
Transmit gain	28.5 dBi
Array aperture	1.8 m
Number of elements	36
Array gain	27 dBi
Receive beamwidth	1.0° × 1.0°
Rotation rate	Up to 20.0° s ⁻¹
Rotation angle	-80.0° to +100°
Pulse length	1–15 μ s
Pulse repetition frequency	1–2,000 Hz
Maximum duty cycle	2%
Maximum pulse bandwidth	5 MHz
Waveform type	Nonlinear frequency modulation
Range resolution	37.5 m
Range gate size	30 m

Field campaign strategies				
Year	Pulse length	Resolution	PRT	Nyquist
2012	1 μ s	150 m	625/938 μ s	v_r not available
2013	9 μ s	45 m	625/938 μ s	v_r not available
2014/15	5.25 μ s	37.5 m	314 μ s	25 m s ⁻¹

compared with existing rapid-scanning radars. While the shallow-volume scanning rates between the radars in Table 1 are roughly equal, the AIR is able to consistently observe the lowest 20° with no gaps in coverage and 1° beams throughout the column, regardless of azimuthal rotation rate. This is a unique capability in this class of rapid-scanning mobile radars, at least in their default modes, although it should be noted that RSDOW has the ability to be upgraded to more beams in the future [to date, a maximum of six concurrent beams has been used with RSDOW (Kosiba and Wurman 2013; Wurman et al. 2014; Wakimoto et al. 2016)]. MWR-05XP can achieve similar sector volumes, albeit at a slightly coarser resolution, and RaXPol requires more time to reach 20° elevation angles without gaps. RSDOW has tunable elevation angles, meaning the user can choose to focus on the low levels of a storm with dense vertical spacing or distribute the available beams throughout the column. RSDOW can also alternate elevation angles from scan to scan, allowing for additional elevations but also adding additional necessary sweeps (J. Wurman 2016, personal communication). The AIR accomplishes its scanning strategy with the use of one primary transmit frequency with minimal bandwidth, potentially leading to less interference with other radars in the X band and more opportunities for multiple-Doppler scanning/analysis, although the tunable nature of RSDOW can also aid in reducing interference. The ability to utilize pulse compression allows the AIR to adjust sensitivities on the fly based on target characteristics and range. Pulse compression is also available to RaXPol and the MWR-05XP but is not available on RSDOW.

Atmospheric imaging, however, comes at the cost of introducing high vertical sidelobe levels in the formed beams. Typically, an antenna will maintain a main beam with tuned sidelobes that drop off quickly beyond the 3-dB point and reach a maximum two-way peak of −25 to −30 dB beyond the main beam (Skolnik 2002). With the use of imaging, the dimension that is being beamformed suffers from higher sidelobes than traditional antennas. The AIR currently yields peak vertical sidelobes of −13.3 dB because of the use of Fourier beamforming. This causes an effective spreading between elevations that is on the order of 10–15 dB worse than typical antennas. Imaging radars also suffer from considerably lower sensitivity than their high-gain, pencil-beam counterparts because the energy from the transmitter is being spread over a wider angle. While much of this loss is made up for with pulse compression, its effects can further complicate attenuation issues in convective weather at X band. The AIR can detect approximately 6, 12, 16, and

18 dBZ at 5, 10, 15, and 20 km, respectively, assuming no hydrometeor-caused attenuation. Finally, the AIR does not possess the capability to provide polarimetric estimates, leading to the lack of ability to discriminate between different hydrometeor types such as rain, hail, and tornadic debris (e.g., Straka et al. 2000; Ryzhkov et al. 2005; Park et al. 2009; Snyder et al. 2013). Of the rapid-scan radars discussed in this paper, only RaXPol retains polarimetric capabilities. For these reasons, the AIR should be viewed as an addition to the current fleet of rapid-scan mobile radars, not a one-size-fits-all solution for rapid-scan weather radar.

DATA COLLECTION EXAMPLES. *19 May 2013, Shawnee, OK.* On 19 May 2013, the AIR collected data on an EF4 tornado near Shawnee, Oklahoma. The AIR was deployed near Tecumseh along Highway 9, with 90° azimuthal sectors and slightly less than 6-s volumetric updates. Data were collected at a closest range of approximately 12 km, with the most intense damage occurring at a similar range. An illustration of a weak echo hole (WEH; Fujita 1981) track at the 2° elevation angle is shown in the top panel of Fig. 2, with the National Weather Service (NWS) damage survey shaded in color underneath (the WEH centers were identified manually; the NWS damage survey can be accessed at <http://apps.dat.noaa.gov/StormDamage/DamageViewer/>). WEHs have been hypothesized to indicate debris centrifuging (Dowell et al. 2005), but they can be used as an approximate tornado center without the availability of v_r data. An animation of the Shawnee tornado data can be accessed at <http://dx.doi.org/10.1175/BAMS-D-15-00266.2>.

The AIR provides the ability to observe rapidly evolving phenomena in time and height, making low-level, quickly evolving features in tornadoes particularly interesting for investigation. One such area for study is the rapid evolution of debris in a tornado. It is important to note that without polarimetric data, the existence of debris (or its density in the tornado) cannot be explicitly determined. However, the AIR was situated serendipitously close to the KTLX (Oklahoma City, OK) Weather Surveillance Radar-1988 Doppler (WSR-88D), offering a close comparison with a polarimetric radar. A tornadic debris signature (TDS) is present in KTLX data during the period highlighted (2330–2340 UTC) with maximum reflectivity factor (Z) exceeding 60 dBZ and minimum copolar cross-correlation coefficient (ρ_{hv}) values below 0.3 (not shown). Additionally, the tornado was causing EF2–EF4 damage during the times investigated (see Fig. 2). These TDS characteristics are consistent with past TDS observations of violent tornadoes and indicate the likelihood for

substantial debris lofting (Ryzhkov et al. 2005; Bodine et al. 2013). While polarimetric radars are becoming more ubiquitous and both fixed (e.g., Bunkers and

Baxter 2011; Schultz et al. 2012; Van Den Broeke 2015) and mobile polarimetric radars have observed TDSs (e.g., Bluestein et al. 2007a; Wurman et al. 2014; Houser et al. 2016), multiple studies have inferred debris characteristics from Z data when polarimetric data were not available (Wurman and Gill 2000; Bluestein et al. 2004; Dowell et al. 2005; Bunkers and Baxter 2011; Wakimoto et al. 2011; Wurman and Kosiba 2013).

As an indication of the potentially increased amounts of debris in the tornadic circulation, the 2° Z field at four different times is shown in the four lower panels of Fig. 2; these times are also marked along the WEH track in the top panel of Fig. 2. At 2330:02 UTC, a mature hook echo with a clearly defined WEH was evident along with EF2 damage indicators. Spiraling bands were apparent to the north and east of the tornado and have previously been shown to mark the potential for debris ejections and precipitation (observations that could benefit from polarized radar for discrimination; Kurdzo et al. 2015). At 2333:47 UTC, after an increase to EF3 damage indicators, the WEH was still apparent but had decreased in size, with higher Z values around the core tornadic circulation. By 2334:23 UTC, during the time of greatest damage according to the NWS damage survey, the WEH had been filled in by even higher Z values as the tornado became loaded with debris. Rapid filling of a WEH was first described in detail by Alexander and Wurman (2005) and was more recently shown by Wakimoto et al. (2015) on the order of 15 s in the 31 May 2013 El Reno, Oklahoma,

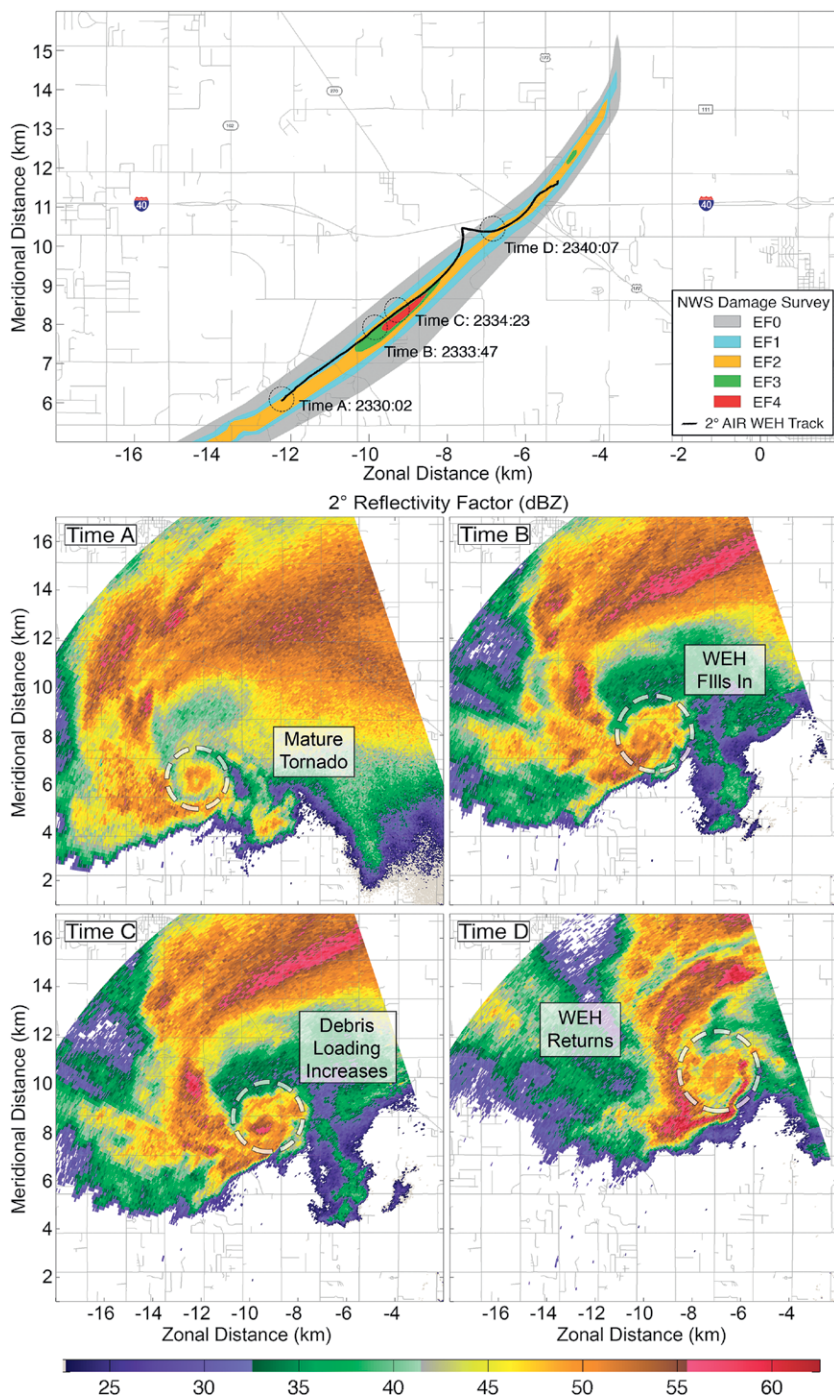


FIG. 2. (top) Observed WEH track at the 2° elevation angle (solid black line), with NWS damage survey contours (colors) from the 19 May 2013 Shawnee, OK, EF4 tornado. (bottom) Z (dBZ) at 2° elevation angle at four selected times (A–D), with distances labeled from the radar location (which is to the southeast of the frame). Times A–D correspond to the circled points along the tracks in the top panel of the figure. Annotations highlight changes in WEH during debris loading stages.

tornado, while an associated TDS (including the use of polarimetric data) had been ongoing and an area of increased damage indicators was evident in a post-tornado damage survey.

To more closely investigate the rapidly evolving three-dimensional nature of Z (and possibly debris) in the Shawnee tornado, a series of five consecutive Z observations at the 1°, 2°, and 3° elevation angles

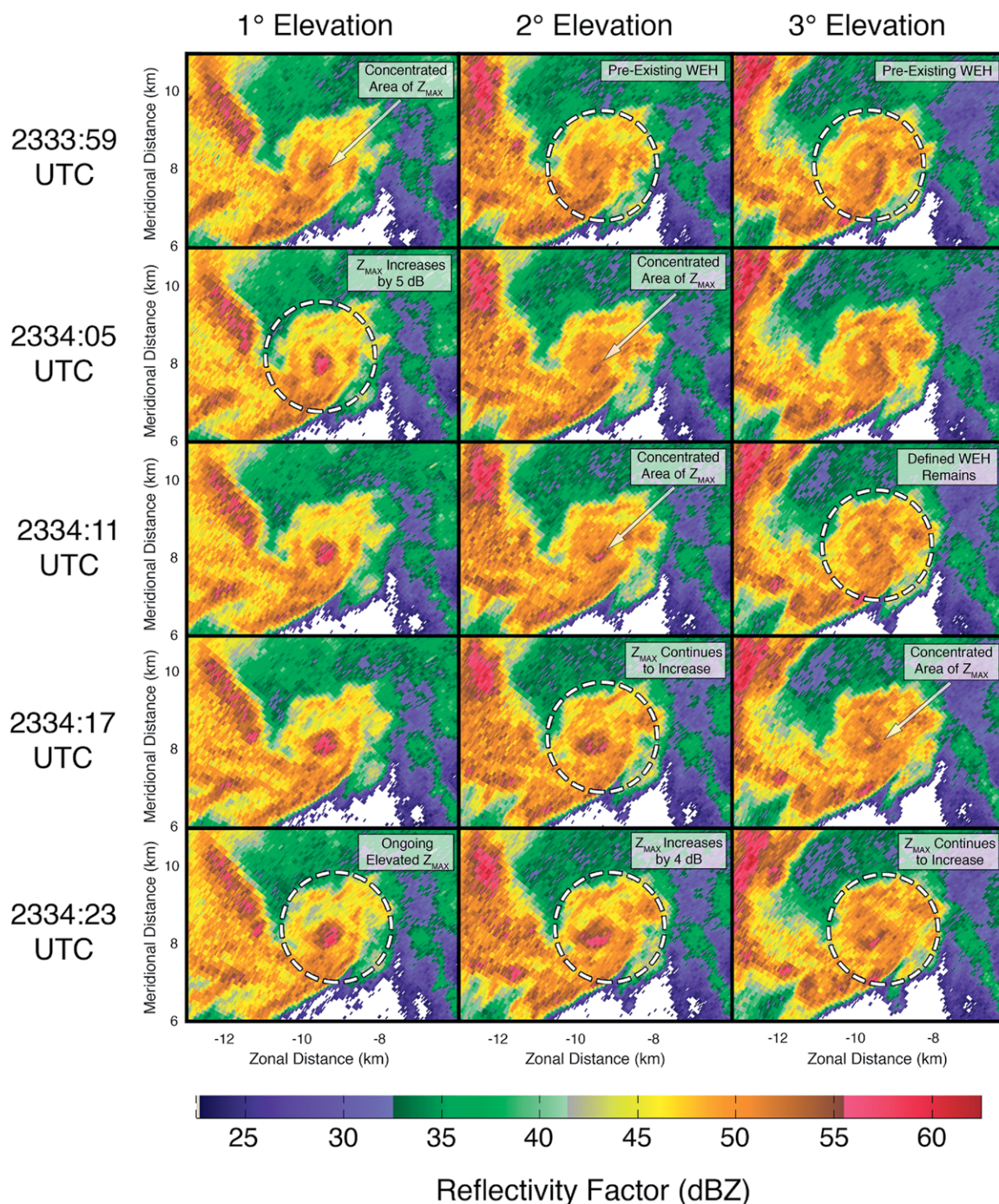


FIG. 3. Z (dBZ) at 1°, 2°, and 3° elevation angles (left to right, respectively) from 2333:59 to 2334:23 UTC (top to bottom, every 6 s) from the 19 May 2013 Shawnee, OK, EF4 tornado. An increase in Z_{MAX} was evident first at the 1° elevation angle, followed by the 2° and 3° elevation angles, respectively. The rapid increases in Z_{MAX} from low elevations to high elevations occurred near the time of maximum damage in the NWS survey and are thought to serve as evidence for rapid lofting of debris in the tornado, despite the lack of polarimetric estimates.

is presented in Fig. 3. At 2333:59 UTC, a small but apparent WEH was evident at the 2° and 3° elevation angles, with the remainder of the tornadic circulation made up of relatively homogenous Z fields. At 1°, in contrast to the uniform Z field at 2° and 3°, a small, concentrated area of elevated Z was apparent, indicating the potential for concentrated debris lofting within a small region. Six seconds later, at 2334:05 UTC, the local maximum Z value (Z_{MAX}) had increased by 5 dB at the 1° elevation angle, or roughly 225 m above ground level (AGL), and a new area of potential concentrated debris lofting was evident at the 2° elevation angle (approximately 440 m AGL). This concentration at higher elevations continued through 2334:17 UTC at 2° and became apparent at the same time at 3° (approximately 660 m AGL). By 2334:23 UTC, Z_{MAX} had increased by 4 dB from the previous time step at 2°, and the area of increased Z was continuing to grow at 3°.

At each elevation and time step, the area of elevated Z occurs on the south and east sides of the WEH and attendant TDS (on KTLX), closer to the EF4 damage indicators and in the area where the translational velocity of the tornado aligns with the tangential wind component. This analysis shows the potential use for rapid volumetric updates at fine vertical resolution at low levels in tornadoes, as well as the need to analyze such features with polarimetric data. In the future, dual-Doppler analysis with another rapid-scanning radar, especially a polarimetric radar, could yield high-resolution wind field analyses that could contribute to a better understanding of the relationship between three-dimensional winds and spatial TDS structure, as well as our understanding of how changing debris distributions affect radar wind measurements (Lewellen et al. 2008; Bodine et al. 2016).

21 May 2014, Denver, CO. The 21 May 2014 Denver, Colorado, supercells were part of a multiday “Denver cyclone” severe weather outbreak (Crook et al. 1990, 1991). While multiple supercellular storms formed over and just east of Denver, one supercell was the primary tornado producer according to reports in the Storm Prediction Center (SPC) database. A number of weak, short-lived, sub-tornado-strength convective storm vortices (SCVs) were apparent in AIR data; additionally, some of the SCVs aligned closely in space and time with SPC tornado reports. The SCV terminology was used by Tanamachi et al. (2013) to describe vortices that appeared similar in nature to tornadic vortices in radar data but without meeting human observer criteria for a tornado. Other similar terms that have been used in the literature include nontornadic vortices (Bluestein et al. 1995) and marginal tornadoes (Wurman and

Kosiba 2013). The SCV terminology is used for this case because the AIR team did not visually observe any tornadoes despite its appropriate location to observe mesocyclonic tornadoes, and no photographs are known to exist of tornadoes at the time of the reports. Additionally, the tornadic differential radial velocity (Δv_r) threshold defined by Alexander and Wurman (2008) of 40 m s⁻¹ was not met in AIR data.

Rear flank gust front surges (RFGFSs) have been shown to have potential impacts on mesocyclone and tornado structure (Adlerman et al. 1999; Finley and Lee 2004; Adlerman and Droegeheimer 2005), and more recent studies have investigated their role in tornadogenesis, tornado maintenance, and tornadic dissipation using mobile radar data (Wurman et al. 2007b; Lee et al. 2012b; Marquis et al. 2012; Kosiba et al. 2013; Kurdzo et al. 2015). Wurman et al. (2007b) utilized dual-Doppler analysis to show anticyclonic rotation and divergence associated with the rear-flank downdraft (RFD) as it wrapped around an existing tornado, while Kosiba et al. (2013) investigated the interaction between primary and secondary RFGFSs in the formation of a tornado. Marquis et al. (2008, 2012) show examples of tornadoes occurring along an RFGFS in the RFD region of a supercell. Skinner et al. (2014, 2015) conducted studies on the role of internal rear flank downdraft momentum surges using mobile radar observations, while Schenkman et al. (2016) took a numerical modeling approach to investigate internal outflow surges. In the case of 21 May 2014, the AIR was able to resolve subtle features that resulted in the rapid genesis and dissipation of multiple SCVs that appeared to be related to ongoing RFGFSs. Eight-second sector volumes were completed using a 130° azimuthal sector, and the AIR was positioned east of the hook by 9 km.

A sample of Z and storm-relative v_r estimates (using manually computed storm motion at the base of the hook) is shown in Fig. 4, with the hook structure in Z shown in the top-left panel. In the top-right panel, an area of RFD winds with a concentrated focus to the south of the developing rotation is visible in the storm-relative v_r field along the southern flank of the hook echo (the RFD area is marked by a translucent arrow). In the bottom panel of Fig. 4, a series of eight storm-relative v_r estimates is shown at 8-s temporal resolution, covering roughly 1 min of time. At 2031:02 UTC, an inbound velocity maximum was located due south of the maximum outbound velocities, with a Δv_r of 20 m s⁻¹. By 2031:19 UTC, an inbound maximum seemingly originating from the ongoing RFGFS became oriented adjacent to the outbound maximum, resulting in an apparent SCV with a Δv_r of 25 m s⁻¹ at

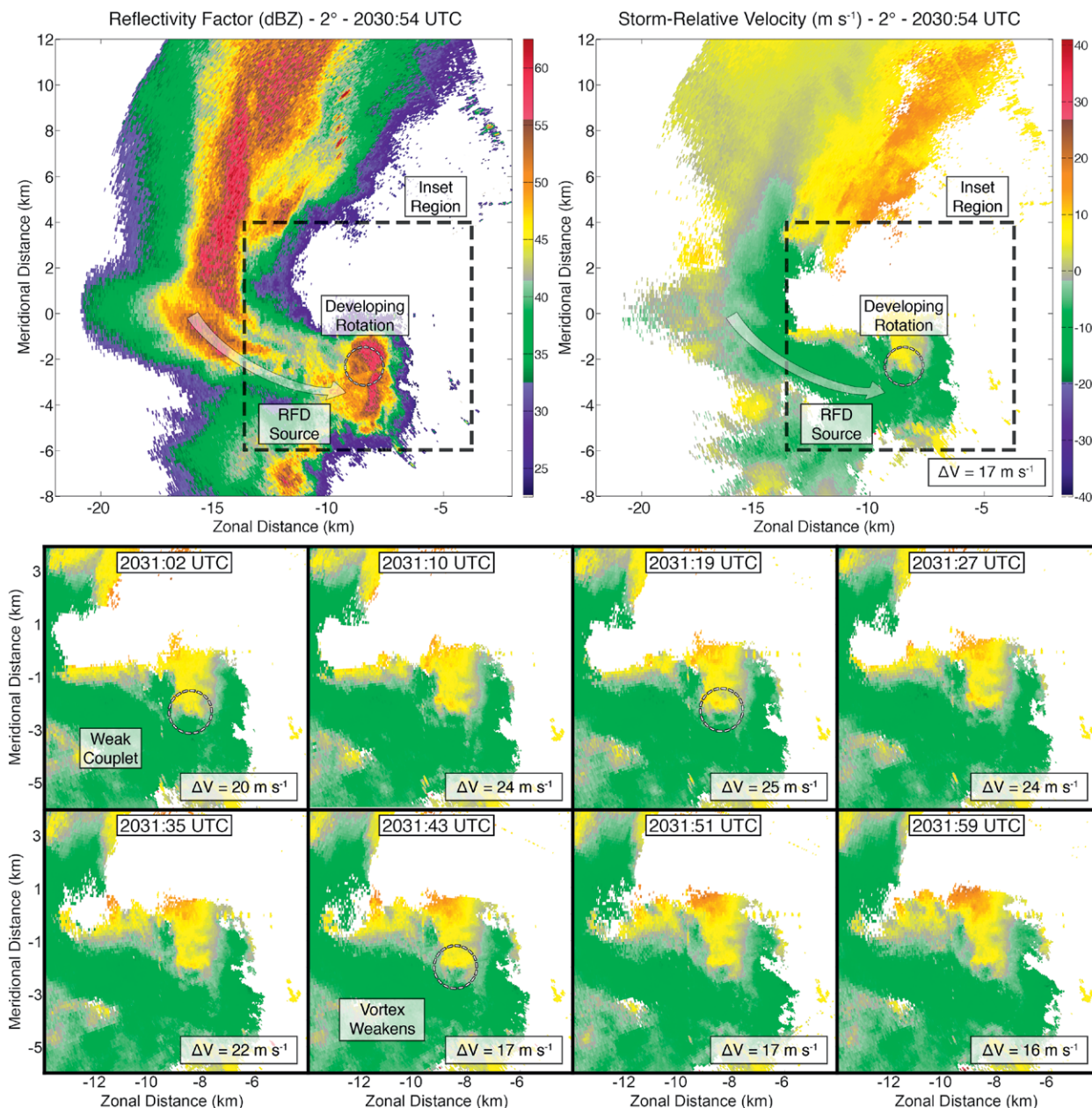


FIG. 4. (top left) Z (dBZ) and (top right) storm-relative v_r (m s^{-1}) at the 2° elevation angle from the 21 May 2014 supercell near Denver, CO. The white arrow depicts the rear flank downdraft area where RFGFSs occurred nearly constantly as evidenced by strong inbound flow in the v_r field just south of the developing rotation. (bottom) v_r (m s^{-1}) showing the development and dissipation of an SCV at 8-s temporal resolution over the span of 1 min. Dashed white circles highlight the SCV center at various stages of strengthening and dissipation.

roughly 292 m AGL; by 2031:43 UTC, this couplet had decreased in intensity to 17 m s^{-1} . The timing of these data match up within 1 min of a tornado report in the SPC database east of Denver associated with the same storm. Considering the fact that the observed SCV was nearly 300 m AGL, it is possible that stronger rotation and an associated tornado were present below the radar beam and out of visual line of sight, resulting in the SPC database report.

16 May 2015, Tipton, OK. On 16 May 2015, the AIR collected data on a strong tornado in southwestern Oklahoma. Deployed 8 km south of Tipton, Oklahoma, a 105° sector was completed with update rates of less than 7 s and a minimum range of 12 km. The tornado was in a mature “wedge” stage (Fig. 5a) during portions of the 35-min deployment. A photograph of the deployment location and parent supercell is shown in Fig. 5b. The Tipton tornado was rated

EF3 by the NWS. An animation of the Tipton tornado data can be accessed at <http://dx.doi.org/10.1175/BAMS-D-15-00266.2>. A sampling of the 5° elevation angle every 4 min during the mature stages of the tornado is shown in Fig. 6. During the Tipton tornado, a series of rapid changes in mesocyclone structure and intensity were evident in AIR data. Multiple instances involved the rapid formation of a secondary mesocyclone (henceforth mesocyclone MB) and its subsequent interaction with the primary/preexisting mesocyclone (mesocyclone MA). Rapid mesocyclogenesis has been observed on the order of 4–8 min previously [perhaps most notably in the 5 June 2009 Goshen County, Wyoming, tornado during the second Verification of the Origins of Rotation in Tornadoes Experiment (VORTEX2); Markowski et al. 2012a,b; Kosiba et al. 2013; Marquis et al. 2014], and some of the most rapid changes observed have occurred on time scales of 1–2 min (Skinner et al. 2014). Cyclic mesocyclogenesis (Burgess et al. 1982) has been observed numerous times (e.g., Beck et al. 2006; Wurman et al. 2007b; French et al. 2008; Houser et al. 2015), although usually such cases are linked to cyclic tornadogenesis rather than occurring during ongoing tornadoes (Dowell and Bluestein 2002a,b; Tanamachi et al. 2012).

The instance with the strongest secondary mesocyclone was observed between approximately 2305 and 2307 UTC, although a similar phenomenon also occurred in the 2302–2304 UTC timeframe (not shown). Rapid intensification of MB took place on the order of 30 s, while the interaction with MA and eventual dissipation of MB took place over a period spanning approximately 90 s. Interference from another X-band transmitter resulted in multipath interference with the AIR, especially in the forward flank region. For this reason, v_r data have been dealiased and subjectively censored in areas where low signal-to-noise ratio and/or interference effects were evident. MB and MA rotations were observed as low as 1° (approximately 200 m AGL), but because of interference and blockage issues, Δv_r is not quantified below the 5° elevation angle. Although a secondary tornado associated with MB was not observed, we do not exclude the possibility that one or more secondary tornadoes occurred, especially given the relatively high Δv_r values.

Following the establishment of MB at 5°, an interaction with MA spanned the following 90 s and is detailed in Fig. 7 with v_r data shown at 7-s increments and MB (MA) markers to the southwest (southeast) of the mesocyclones. The term “interaction” is used in the

sense that the two mesocyclones were relatively close to each other and changes in intensity and direction of both mesocyclones seemed to be correlated in time. At 2305:33 UTC, MB can be seen approximately 1.5 km north-northwest of MA, with MA exhibiting a relatively strong, symmetric structure above the ongoing tornado. By 2305:47 UTC, MB had increased in intensity, and by 2305:54 UTC, MA had decreased in intensity, while the separation between MB and MA had decreased to 1 km. Over the following 20 s, MB continued to intensify and move south while MA continued to weaken and move northeast. Between 2306:21 and 2306:28 UTC, MB exhibited its strongest inbound velocities, while MA exhibited its weakest



FIG. 5. (a) The 16 May 2015 Tipton, OK, EF3 tornado looking to the south-southwest (photograph courtesy of Jeffrey Snyder). (b) The AIR’s view of the 16 May 2015 storm looking toward the north-northwest [image has been contrast stretched for better clarity (Jain 1989)].

inbound velocities. This may be due to the attendant outbound velocities associated with the eastern side of MB interfering with the inbound velocities of MA, as the outbound velocities of MA appear to remain at similar strength throughout the period of investigation. By 2306:34 UTC, MB had established itself southwest of MA and had begun to weaken. In the final two frames, MB began to rotate around MA, resulting in a sharp northerly turn by MA, along with reintensification. It should be noted that during the time of interaction between MB and MA, it is difficult to tell which area of inbound velocities is related to each mesocyclone, making it difficult to perform a fair Δv_r analysis of each mesocyclone separately during this period.

Tornadic decay has been associated with the RFD structure of a mesocyclone moving outflow-driven air around the updraft/tornado (Brandes 1978; Lemon and Doswell 1979; Markowski 2002; Marquis et al. 2012), while cyclic mesocyclogenesis occasionally takes on a nonoccluding mode (Adlerman and Droegemeier 2005), where an ongoing mesocyclone may continue while a new mesocyclone forms in the hook region. While the inbound velocities associated with MB did eventually act similar in nature to an RFGFS or an internal momentum surge (i.e., strong, localized near-surface winds within the expected RFD region of the supercell; e.g., Markowski et al. 2002; Finley and Lee 2004; Wurman et al. 2007b; Lee et al. 2012a; Skinner et al. 2014, 2015), causing an apparent weakening and turning of MA, the tornado continued for another 30 min without significant disruption. Although not shown, it is relevant to note that in the 1–2 min prior to the MA–MB interaction, the storm-scale tilt of MA (between 500 m and 2 km) tripled (from 10° to 30°) before rapidly recovering. Collection of simultaneous elevations could make analysis of such rapid changes easier to relate to a phenomenon such as the MA–MB interaction.

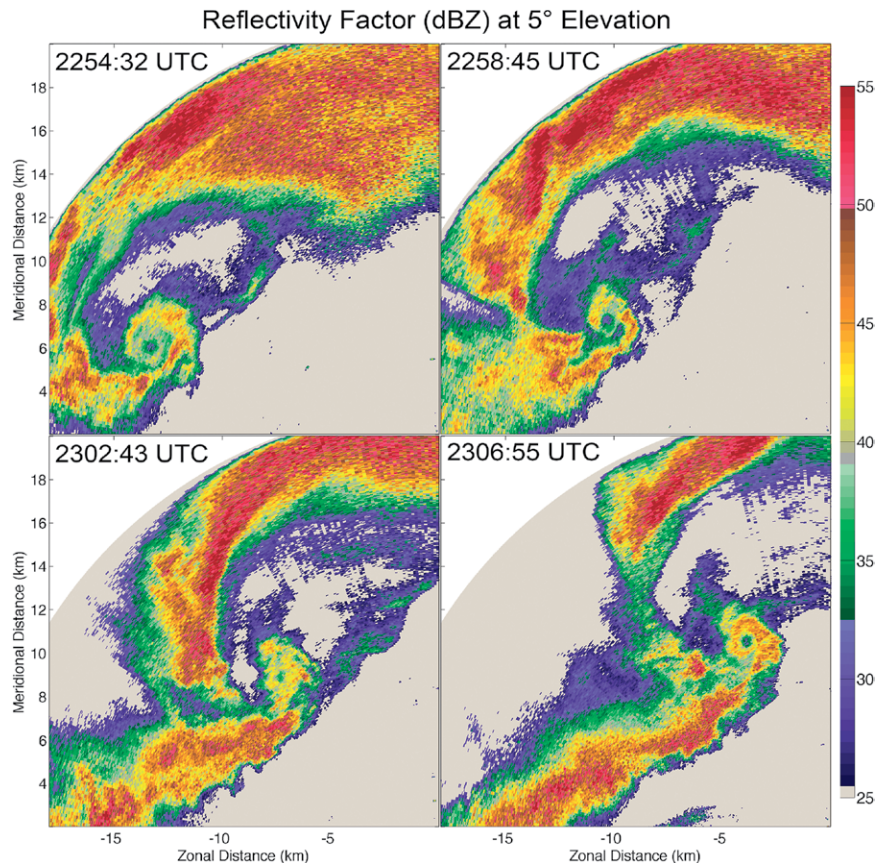


FIG. 6. Z (dBZ) at the 5° elevation angle from four times throughout the 16 May 2015 Tipton, OK, EF3 tornado, spanning from 2254:32 to 2306:55 UTC at roughly 4-min resolution. The tornado, marked by the WEH in the hook region, traversed the scanning sector, resulting in a dataset that spanned 35 min.

Rapid mesocyclogenesis and mesocyclone maintenance and dissipation have potential impacts on real-time forecasting and warning efforts. With efforts such as the multifunction phased array radar (MPAR; Weber et al. 2007; Zrnić et al. 2007) and collaborative adaptive sensing of the atmosphere (CASA; McLaughlin et al. 2009) focusing on rapid updates for forecasters, a clearer understanding of these rapid changes could be useful to forecasters once a new national radar network with rapid scanning is in place. Volumetric multi-Doppler with two or more rapid-scanning radars could have better resolved the intensification stages of MB and potentially allowed for separation between MB and MA in the interaction stages to determine their relative strengths and rapid evolution, leading to a better understanding of how this interaction affected mesocyclone maintenance and changes in intensity and direction.

27 May 2015, Canadian, TX. The 27 May 2015 Canadian, Texas, tornado occurred along a dryline in a high-convective available potential energy (CAPE),

Radial Velocity (m s^{-1}) at 5° Elevation

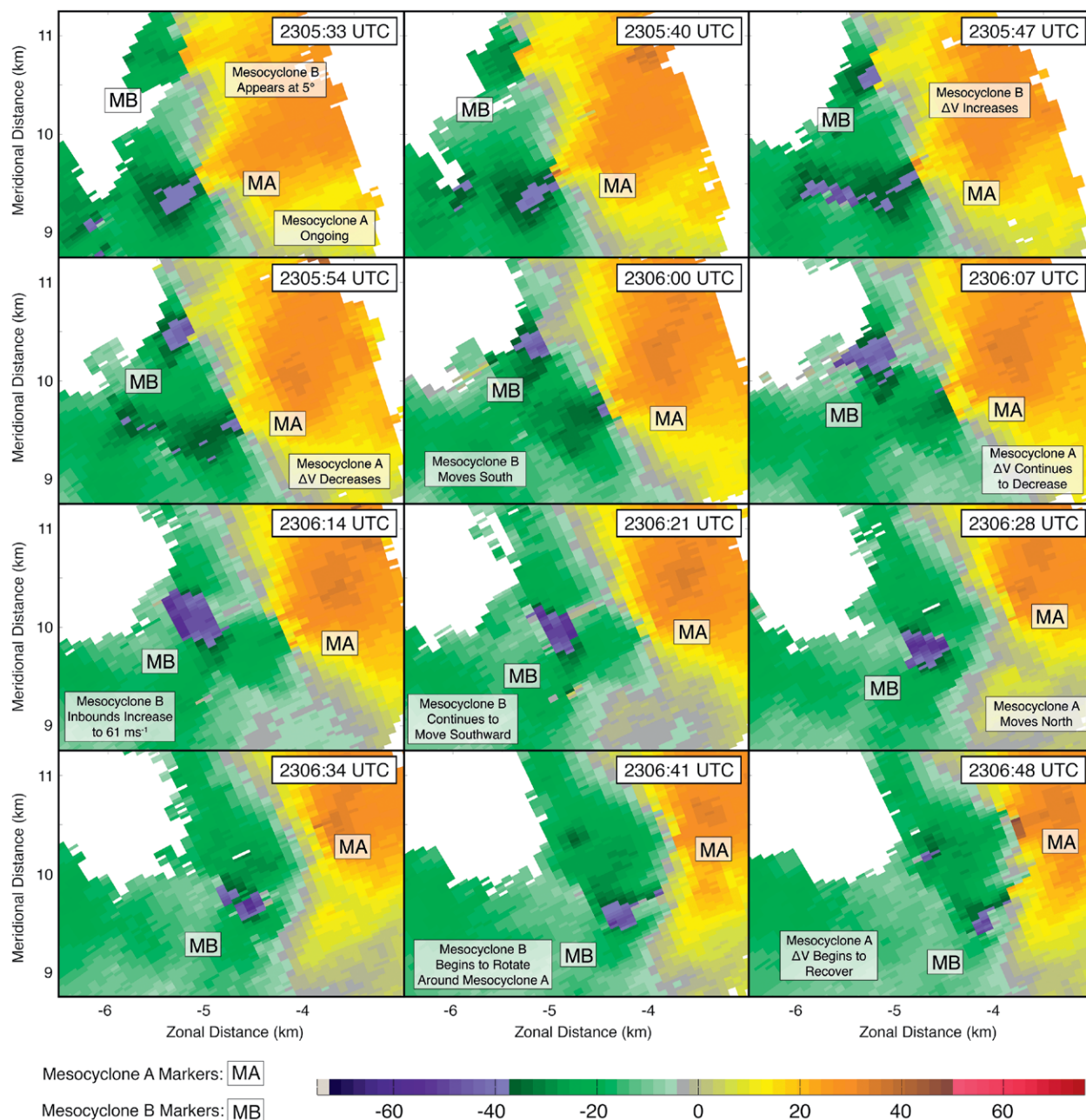


FIG. 7. v_r (m s^{-1}) at the 5° elevation angle, spanning from 2305:33 to 2306:48 UTC from the 16 May 2015 Tipton, OK, EF3 tornado at roughly 7-s resolution. The primary mesocyclone and secondary mesocyclone are labeled “MA” and “MB,” respectively. Between 2305:33 and 2306:07 UTC, MB strengthened considerably while moving southward, as MA appeared to weaken and move northeastward. Between 2306:14 and 2306:41 UTC, MA and MB interacted, with the outbounds from MB appearing to counteract the inbounds of MA. By 2306:48 UTC, MB had moved south of MA and had begun to weaken, while MA had taken a turn toward the north and restrengthened.

low-shear environment. The AIR was deployed 4 km north-northeast of Canadian and captured the mature and dissipation stages of a cone tornado that had little forward ground motion. The primary AIR deployment was 6 min long and covered an 80°

sector with a 5.5-s update rate, and the closest range to the tornado was 6 km. The Canadian tornado was rated EF2 by the NWS. Rapid changes in vortex shape and tilt were observed visually as the tornado transitioned from a cone to a highly tilted rope stage;

this progression is shown in Fig. 8. An animation of the Canadian tornado data can be accessed at <http://dx.doi.org/10.1175/BAMS-D-15-00266.2>.

A sampling of Z and manually dealiased v_r at 0° elevation angle (a beam height of roughly 75 m AGL at the tornado's location, accounting for up to 0.5° of error in the elevation estimate and a slightly elevated scanning location) is shown in Fig. 9 at approximately 11-s temporal resolution in order to demonstrate the change in tornadic structure during the dissipation stages. Early in the deployment, at 2203:52 UTC (top panel

of Fig. 9), the tornado was in its mature stage with a WEH over 1 km in diameter. A photograph at the beginning of the deployment is shown in Fig. 8a. The inbound and outbound maxima were separated by nearly 1 km, indicating a large and strong tornado. The total Δv_r spanned over 10 radials and equated to roughly 90 m s^{-1} close to ground level. Low radial velocities in the tornadic core imply that there were large radial gradients of tangential velocity in the corner flow region. Tangential velocities in this region are proportional to swirl ratio, indicating a relatively high swirl ratio at this stage of the tornado's life cycle (Davies-Jones 1986).

Just 10 s later, the WEH had narrowed considerably in the Z field, but a wide vortex continued in the v_r field (see Fig. 9a). The WEH became less organized after the first two scans, and as discussed in the Shawnee case previously, rapid changes in WEH definition have been documented previously (Wakimoto et al. 2015). This weakening trend continued over the next 4 min, with maximum Δv_r decreasing by more than 50 m s^{-1} in under 3 min. However, the high temporal resolution of the AIR exposed more rapid changes in the WEH and v_r fields. At 2204:13 UTC (Fig. 9b), the inbound v_r maximum began to move radially inward toward the radar location while subsequently weakening in intensity. Additionally, an anticyclonic couplet appeared in v_r data to the north of the tornado. By 2204:24 UTC (Fig. 9c), the WEH had lost much of its shape and the maximum

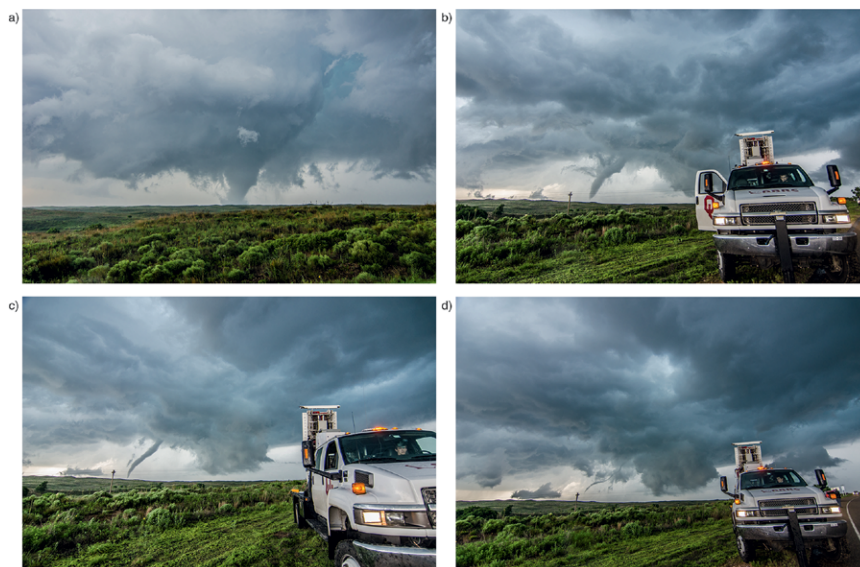


FIG. 8. Comparison of tornado structure during the AIR deployment on the Canadian, TX, EF2 tornado on 27 May 2015. Approximate times for the images are (a) 2204, (b) 2207, (c) 2208, and (d) 2209 UTC. Images have been contrast stretched for better clarity (Jain 1989).

Δv_r had decreased roughly 30 m s^{-1} in 11 s, while the anticyclonic couplet continued to intensify. At 2204:35 UTC (Fig. 9d), just 43 s after the peak WEH width and Δv_r , the WEH had decreased to less than 0.5 km in width and the inbound v_r had separated nearly 1 km from its previous position relative to the outbound v_r maxima. The anticyclonic couplet reached a maximum intensity, with Δv_r near 50 m s^{-1} , although a secondary tornado was not observed. A series of possible secondary funnels were evident visually, but the lack of a tornado makes the SCV designation appropriate for the anticyclonic couplet. The SCV weakened to less than 30 m s^{-1} by 2204:45 UTC and was no longer apparent by 2204:51 UTC (not shown).

To investigate the volumetric characteristics of the Canadian tornado, a series of three-dimensional spatial analysis points during the dissipation stage were chosen and analyzed, with the result shown in Fig. 10a. A Z contour was applied in order to visualize the three-dimensional structure of the WEH (in this case, a 36-dBZ contour was chosen). Without temperature, humidity, and pressure/wind fields in three dimensions, a “condensation” funnel cannot be visualized, meaning that the WEH is not a true physical representation of the tornado or updraft. However, centrifuging theory does argue that the center of the WEH is the center of the vortex, meaning that a tight threshold for contouring does give useful visual information for tilt characteristics. Additionally,

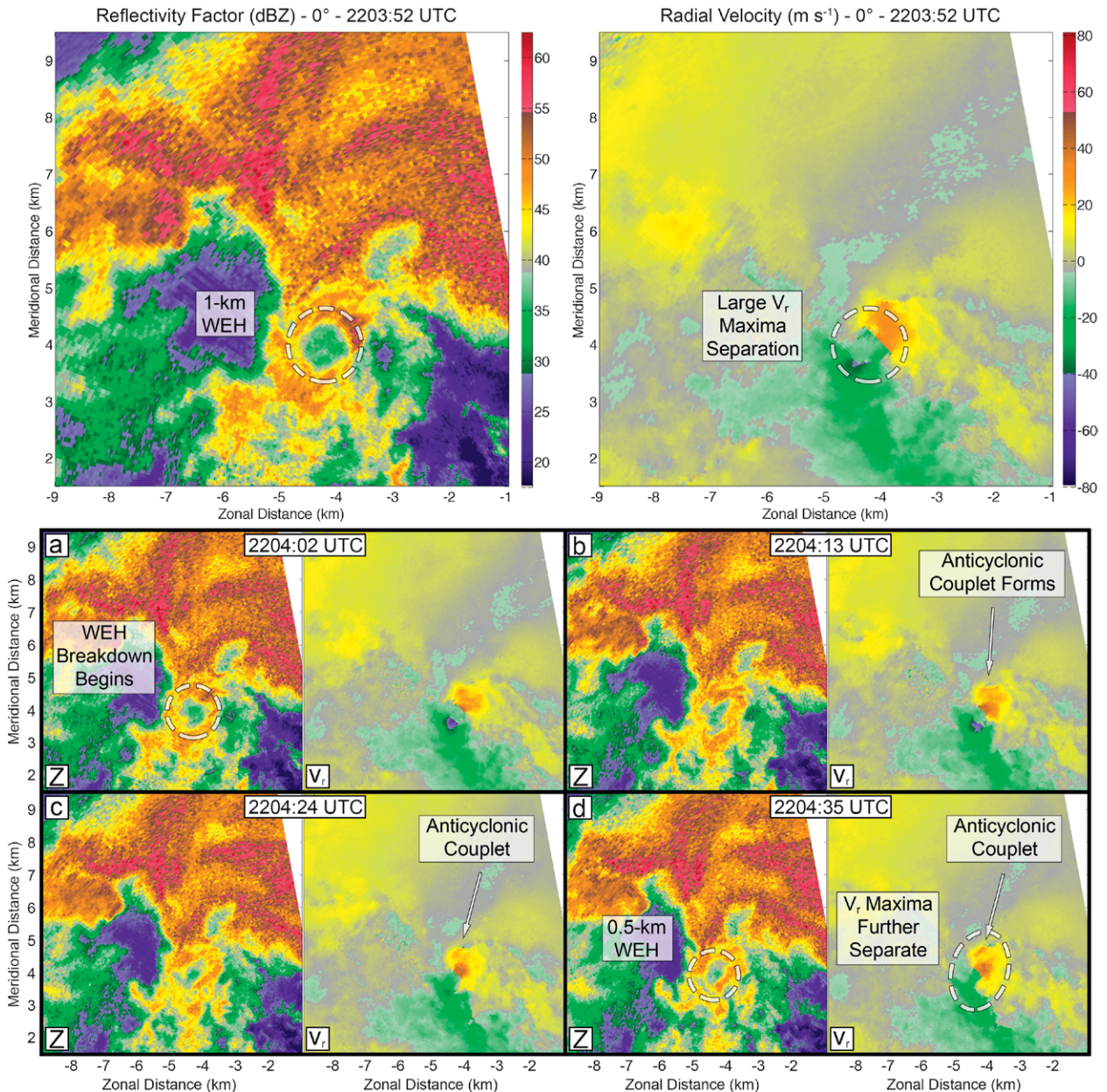


FIG. 9. (top) Z (dBZ) and v_r (m s^{-1}) during the mature stage of the 27 May 2015 Canadian, TX, EF2 tornado (0° elevation angle). (bottom) Z (dBZ) and v_r (m s^{-1}) at 11-s temporal resolution as the WEH began to break down and the inbound v_r maximum transitioned toward the southeast, indicating weakening and a reversal of direction. An anticyclonic couplet is also marked to the north of the tornadic circulation.

radar reflectivity and funnel size, including WEHs, have been illustrated using mobile radar and photogrammetry techniques (e.g., Wakimoto et al. 2011; Atkins et al. 2012; Wakimoto et al. 2012, 2015), although such techniques are generally limited to the visual regions below the updraft base. At this time, the tilt of the tornado was in line with the direction of motion, despite the slow forward speed (i.e., similar to Lewellen et al. 1997). The vertical structure of rotation during tornadogenesis and tornadic dissipation

has been the subject of numerous previous studies (French et al. 2013; Skinner et al. 2014; Houser et al. 2015), including pseudovorticity isosurface analysis in the 24 May 2011 El Reno tornado with RaXPOL (Houser et al. 2015), where rapid development of vorticity throughout the column was observed within one 17-s volume scan. French et al. (2013) investigated the vertical development of tornadic vortex signatures with the MWR-05XP. The MWR-05XP has also been used for isosurface analysis of

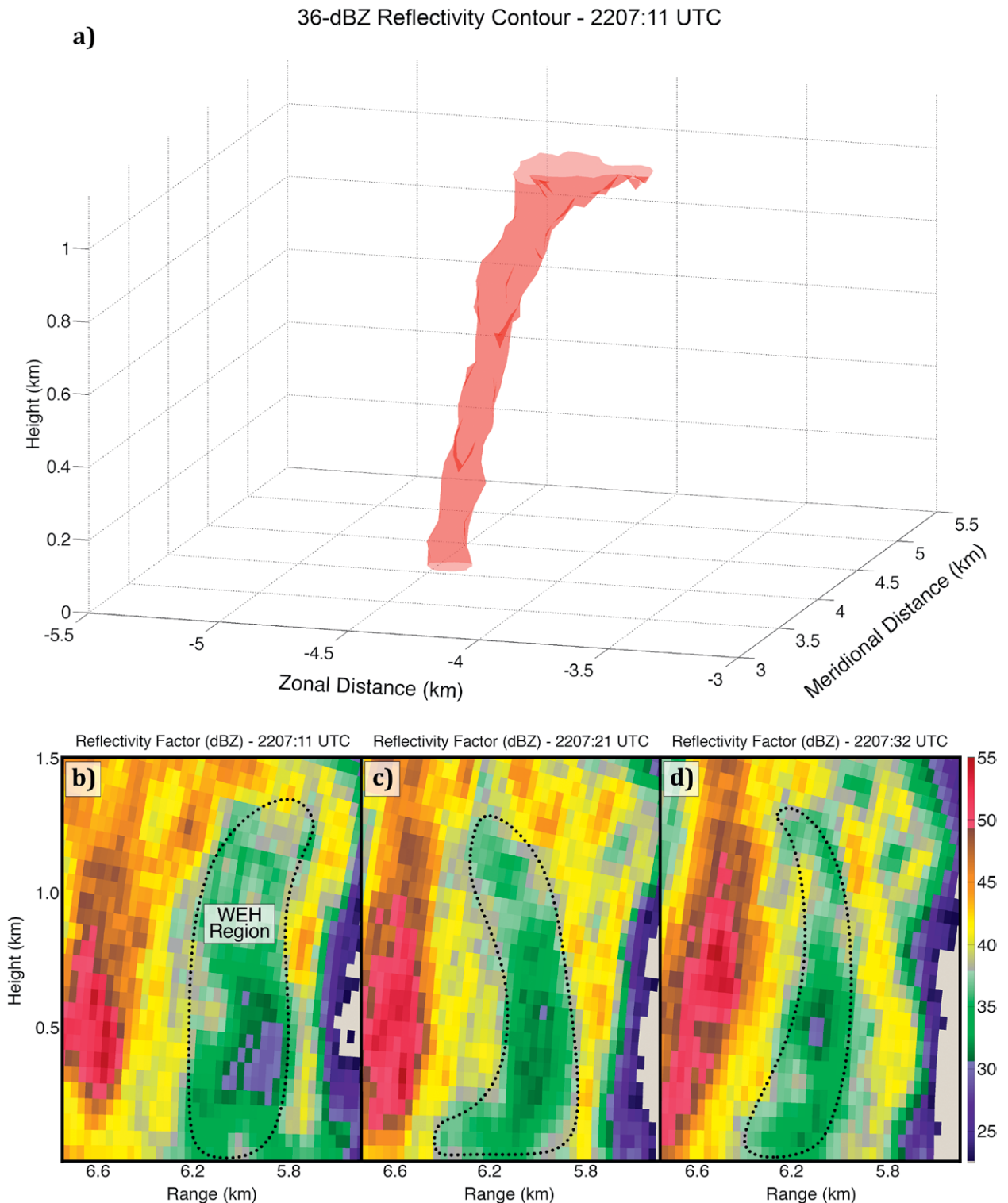


FIG. 10. (a) Three-dimensional 36-dBZ Z isosurface near the WEH of the 27 May 2015 Canadian, TX, EF2 tornado at 2207:11 UTC. (b)–(d) Z RHIs through the tornado at 10.5-s resolution during tornadic dissipation. Vertical extent of the WEH is highlighted by the dotted black line.

vertical vorticity in tornadogenesis cases (Skinner et al. 2015). Fewer studies have examined rapid volumetric dissipation of tornadoes (French et al. 2014),

although the RaXPol did collect dissipation data on a separate tornado on 24 May 2011 (French et al. 2013; Houser et al. 2015).

A series of RHIs through the WEH (at 311° relative to north) starting at the same time as Fig. 10a is shown in Figs. 10b–d. Changes in the Z gradient within the WEH in Fig. 10b can be seen in the vertical dimension, with larger gradients at the 300–500-m layer, followed by smaller gradients and increased tilt near the 1-km height. In Figs. 10c and 10d, the WEH becomes thinner over a time period of 10–20 s, with rapid changes in tilt direction and Z differential in the range dimension. These observations agree with the highly tilted rope stages shown in Figs. 8b–d. Wurman et al. (1996) hypothesized that the WEH could result from a combination of centrifuging and subsidence, meaning that a large WEH during a mature tornado might be due to a large central downdraft inhibiting debris lofting. The smaller WEH observed during the dissipation stages may result from a smaller central downdraft. RHIs through strong tornadoes are rare, since there is a desire to scan volumetrically, and with a 5.5-s update rate, visual depictions of the Canadian tornado can be made in three dimensions nearly 50 times throughout the dissipation stage. RHIs through tornadoes have been presented previously (Wurman and Samaras 2004; Alexander and Wurman 2005; Bluestein et al. 2007b), but required the selection of a pure RHI scanning mode. RSDOW has the capability to produce similar RHIs through tornadoes, especially if a 12-beam mode were to be utilized, although the continuous 20° nature of the AIR observations provides useful additional detail. The combination of RHIs from multiple angles of a tornado could yield the potential for detailed studies of tornado structure simultaneously in the vertical dimension, especially since the dynamic nature of tornadoes requires rapid updates volumetrically in order to create an accurate portrayal of vertical structure.

CONCLUSIONS AND FUTURE WORK. The AIR is capable of scanning severe local storms and other meteorological phenomena at high spatial and temporal resolution, with a specific focus on simultaneous RHI scanning with continuous beams in the vertical dimension. Using this technique, known as imaging, three-dimensional sector volumes can be formed in a $90^\circ \times 20^\circ$ sector in under 6 s. This type of scanning allows for continuous volumetric analysis on short time scales of a variety of meteorological phenomena. Additionally, imaging in the vertical dimension allows for RHI analysis through different areas of the storm of interest at high temporal resolution. RHI analysis with dish antennas is limited to specific scanning modes only, meaning that phased

arrays such as MWR-05XP, RSDOW, and the AIR allow for increased flexibility after data collection is complete.

A series of severe local storm and tornado cases has been presented in order to demonstrate the capabilities of the AIR. These analyses show changes in tornado and storm-scale structure on the order of 5–10 s, including changes in reflectivity structure likely associated with debris, rapid intensification and dissipation of mesocyclones and vortices, and an instance of transition from a large tornado to a rope stage with rapid changes in tornado structure and intensity, as well as the formation/dissipation of an anticyclonic couplet spanning less than 30 s. Many of these observations have been made previously in the literature, but the AIR's ability to focus on rapid time scales in both horizontal space and height makes it an important addition to the existing fleet of mobile radars. Future work for these cases involves the examination of rapidly changing speeds and depths of RFGFSs, storm feature tracking (e.g., debris clouds, downdraft cores, velocity retrievals, and hydrometeor continuity in space and time), and vertical distribution of velocity in the mature and dissipation stages of tornadoes.

Numerous additional data collection types are planned/desired in future field campaigns. Of primary interest is collection of tornadogenesis in multiple cases in order to examine the vertical distribution of velocity at high spatial and temporal resolution. This type of data would assist in validating the work by French et al. (2013) regarding top-down versus bottom-up tornadogenesis. Future collaboration with other rapid-scanning radars could yield high temporal resolution volumetric dual-Doppler data to examine these types of problems. Imaging applications could be of potential use to the MPAR program, especially with the desire to use multiple simultaneous beams (Weber et al. 2007; Zrnić et al. 2007). With a wide variety of cases collected by the AIR, the trade-offs for this technique can be assessed, allowing for the consideration of digital beamforming for use in a future national network of rapid-scanning radars. Finally, the desire to observe rapidly evolving phenomena with polarimetric capabilities has driven recent National Science Foundation funding for a mobile, C-band polarimetric AIR, or PAIR. In the future, the PAIR will be capable of determining three-dimensional structure of tornadoes and debris, observing hurricane dynamics with better attenuation and higher sensitivity, and electronic beam steering for volumetric scanning in less than 3 s.

ACKNOWLEDGMENTS. The authors thank the three anonymous reviewers who offered tremendously helpful reviews of the first version of the manuscript, leading to a much clearer final article. The authors would also like to thank Bradley Isom, Redmond Kelley, John Meier, Matthew McCord, Jonathan Christian, Mark Yeary, and Tian-You Yu for their assistance in the original design, maintenance, and operation of the Atmospheric Imaging Radar. Discussions with Howard Bluestein, Kyle Thiem, Zachary Weinhoff, Jeffrey Snyder, and Casey Griffin were instrumental in data analysis and interpretation. Bryan Putnam and Derek Stratman assisted with forecasting and deployment preparation. This work was supported by CIMMS Cooperative Agreement NA11OAR4320072 and National Science Foundation Grant AGS-1303685. James M. Kurdzo is currently an MIT Lincoln Laboratory employee; no Laboratory funding or resources were used to produce the results/findings reported in this publication.

REFERENCES

- Adachi, T., K. Kusunoki, S. Yoshida, K. Arai, and T. Ushio, 2016: High-speed volumetric observation of wet microburst using X-band phased array weather radar in Japan. *Mon. Wea. Rev.*, **144**, 3749–3765, doi:10.1175/MWR-D-16-0125.1.
- Adlerman, E. J., and K. K. Droegemeier, 2005: The dependence of numerically simulated cyclic mesocyclogenesis upon environmental vertical wind shear. *Mon. Wea. Rev.*, **133**, 3595–3623, doi:10.1175/MWR3039.1.
- , —, and R. Davies-Jones, 1999: A numerical simulation of cyclic mesocyclogenesis. *J. Atmos. Sci.*, **56**, 2045–2069, doi:10.1175/1520-0469(1999)056<2045:ANSOCM>2.0.CO;2.
- Alexander, C. R., and J. Wurman, 2005: The 30 May 1998 Spencer, South Dakota, storm. Part I: The structural evolution and environment of the tornadoes. *Mon. Wea. Rev.*, **133**, 72–97, doi:10.1175/MWR-2855.1.
- , and —, 2008: Updated mobile radar climatology of supercell tornado structures and dynamics. *24th Conf. on Severe Local Storms*, Savannah, GA, Amer. Meteor. Soc., 19.4. [Available online at https://ams.confex.com/ams/24SLS/techprogram/paper_141821.htm.]
- Atkins, N. T., A. McGee, R. Ducharme, R. M. Wakimoto, and J. Wurman, 2012: The LaGrange tornado during VORTEX2. Part II: Photogrammetric analysis of the tornado combined with dual-Doppler radar data. *Mon. Wea. Rev.*, **140**, 2939–2958, doi:10.1175/MWR-D-11-00285.1.
- Beck, J. R., J. L. Schroeder, and J. M. Wurman, 2006: High-resolution dual-Doppler analyses of the 29 May 2001 Kress, Texas, cyclic supercell. *Mon. Wea. Rev.*, **134**, 3125–3148, doi:10.1175/MWR3246.1.
- Bluestein, H. B., and A. L. Pazmany, 2000: Observations of tornadoes and other convective phenomena with a mobile, 3-mm wavelength, Doppler radar: The spring 1999 field experiment. *Bull. Amer. Meteor. Soc.*, **81**, 2939–2951, doi:10.1175/1520-0477(2000)081<2939:OOTAOC>2.3.CO;2.
- , —, J. C. Galloway, and R. E. McIntosh, 1995: Studies of the substructure of severe convective storms using a mobile 3-mm-wavelength Doppler radar. *Bull. Amer. Meteor. Soc.*, **76**, 2155–2169, doi:10.1175/1520-0477(1995)076<2155:SOTSOS>2.0.CO;2.
- , C. C. Weiss, and A. L. Pazmany, 2003: Mobile Doppler radar observations of a tornado in a supercell near Bassett, Nebraska, on 5 June 1999. Part I: Tornadogenesis. *Mon. Wea. Rev.*, **131**, 2954–2967, doi:10.1175/1520-0493(2003)131<2954:MDROOA>2.0.CO;2.
- , —, and —, 2004: The vertical structure of a tornado near Happy, Texas, on 5 May 2002: High-resolution, mobile, W-band, Doppler radar observations. *Mon. Wea. Rev.*, **132**, 2325–2337, doi:10.1175/1520-0493(2004)132<2325:TVSOAT>2.0.CO;2.
- , M. M. French, R. L. Tanamachi, S. Frasier, K. Hardwick, F. Junyent, and A. L. Pazmany, 2007a: Close-range observations of tornadoes in supercells made with a dual-polarization, X-band, mobile Doppler radar. *Mon. Wea. Rev.*, **135**, 1522–1543, doi:10.1175/MWR3349.1.
- , C. C. Weiss, M. M. French, E. M. Holthaus, R. L. Tanamachi, S. Frasier, and A. L. Pazmany, 2007b: The structure of tornadoes near Attica, Kansas, on 12 May 2004: High-resolution, mobile, Doppler radar observations. *Mon. Wea. Rev.*, **135**, 475–506, doi:10.1175/MWR3295.1.
- , M. M. French, I. PopStefanija, R. T. Bluth, and J. B. Knorr, 2010: A mobile, phased-array Doppler radar for the study of severe convective storms. *Bull. Amer. Meteor. Soc.*, **91**, 579–600, doi:10.1175/2009BAMS2914.1.
- , and Coauthors, 2014: Radar in atmospheric sciences and related research: Current systems, emerging technology, and future needs. *Bull. Amer. Meteor. Soc.*, **95**, 1850–1861, doi:10.1175/BAMS-D-13-00079.1.
- Bodine, D. J., M. R. Kumjian, R. D. Palmer, P. L. Heinselman, and A. V. Ryzhkov, 2013: Tornado damage estimation using polarimetric radar. *Wea. Forecasting*, **28**, 139–158, doi:10.1175/WAF-D-11-00158.1.
- , T. Maruyama, R. D. Palmer, C. J. Fulton, H. B. Bluestein, and D. C. Lewellen, 2016: Sensitivity of tornado dynamics to soil debris loading. *J. Atmos. Sci.*, **73**, 2783–2801, doi:10.1175/JAS-D-15-0188.1.

- Brandes, E. A., 1978: Mesocyclone evolution and tornadogenesis: Some observations. *Mon. Wea. Rev.*, **106**, 995–1011, doi:10.1175/1520-0493(1978)106<0995:MEATSO>2.0.CO;2.
- Brown, R. A., V. T. Wood, R. M. Steadham, R. R. Lee, B. A. Flickinger, and D. Sirmans, 2005: New WSR-88D volume coverage pattern 12: Results of field tests. *Wea. Forecasting*, **20**, 385–393, doi:10.1175/WAF848.1.
- Bunkers, M. J., and M. A. Baxter, 2011: Radar tornadic debris signatures on 27 April 2011. *Electron. J. Oper. Meteor.*, **12** (7), 1–6.
- Burgess, D. W., V. T. Wood, and R. A. Brown, 1982: Mesocyclone evolution statistics. *Preprints, 12th Conf. on Severe Local Storms*, San Antonio, TX, Amer. Meteor. Soc., 422–424.
- Cheong, B. L., R. D. Palmer, T.-Y. Yu, K.-F. Yang, M. W. Hoffman, S. J. Frasier, and F. J. Lopez-Dekker, 2008: Effects of wind field inhomogeneities on Doppler beam swinging revealed by an imaging radar. *J. Atmos. Oceanic Technol.*, **25**, 1414–1422, doi:10.1175/2007JTECHA969.1.
- Crook, N. A., T. L. Clark, and M. W. Moncrieff, 1990: The Denver cyclone. Part I: Generation in low Froude number flow. *J. Atmos. Sci.*, **47**, 2725–2742, doi:10.1175/1520-0469(1990)047<2725:TDCPIG>2.0.CO;2.
- , —, and —, 1991: The Denver cyclone. Part II: Interaction with the convective boundary layer. *J. Atmos. Sci.*, **48**, 2109–2126, doi:10.1175/1520-0469(1991)048<2109:TDCPII>2.0.CO;2.
- Crum, T., and R. Alberty, 1993: The WSR-88D and the WSR-88D Operational Support Facility. *Bull. Amer. Meteor. Soc.*, **74**, 1669–1687, doi:10.1175/1520-0477(1993)074<1669:TWATWO>2.0.CO;2.
- Davies-Jones, R. P., 1986: Tornado dynamics. *Thunderstorm Morphology and Dynamics*, Vol. 2, E. Kessler, Ed., University of Oklahoma Press, 197–236.
- Dowell, D. C., and H. B. Bluestein, 2002a: The 8 June 1995 Mclean, Texas, storm. Part I: Observations of cyclic tornadogenesis. *Mon. Wea. Rev.*, **130**, 2626–2648, doi:10.1175/1520-0493(2002)130<2626:TJMTSP>2.0.CO;2.
- , and —, 2002b: The 8 June 1995 Mclean, Texas, storm. Part II: Cyclic tornado formation, maintenance, and dissipation. *Mon. Wea. Rev.*, **130**, 2649–2670, doi:10.1175/1520-0493(2002)130<2649:TJMTSP>2.0.CO;2.
- , C. R. Alexander, J. M. Wurman, and L. J. Wicker, 2005: Centrifuging of hydrometeors and debris in tornadoes: Radar-reflectivity patterns and wind-measurement errors. *Mon. Wea. Rev.*, **133**, 1501–1524, doi:10.1175/MWR2934.1.
- Finley, C. A., and B. D. Lee, 2004: High resolution mobile mesonet observations of RFD surges in the June 9 Basset, Nebraska supercell during Project ANSWERS 2003. *22nd Conf. on Severe Local Storms*, Hyannis, MA, Amer. Meteor. Soc., P11.3. [Available online at https://ams.confex.com/ams/11aram22sls/techprogram/paper_82005.htm.]
- Frame, J., P. Markowski, Y. Richardson, J. Straka, and J. Wurman, 2009: Polarimetric and dual-Doppler radar observations of the Lipscomb county, Texas, supercell thunderstorm on 23 May 2002. *Mon. Wea. Rev.*, **137**, 544–561, doi:10.1175/2008MWR2425.1.
- French, M. M., H. B. Bluestein, D. C. Dowell, L. J. Wicker, M. R. Kramar, and A. L. Pazmany, 2008: High-resolution, mobile Doppler radar observations of cyclic mesocyclogenesis in a supercell. *Mon. Wea. Rev.*, **136**, 4997–5016, doi:10.1175/2008MWR2407.1.
- , —, I. PopStefanija, C. A. Baldi, and R. T. Bluth, 2013: Reexamining the vertical development of tornadic vortex signatures in supercells. *Mon. Wea. Rev.*, **141**, 4576–4601, doi:10.1175/MWR-D-12-00315.1.
- , —, —, —, and —, 2014: Mobile, phased-array, Doppler radar observations of tornadoes at X band. *Mon. Wea. Rev.*, **142**, 1010–1036, doi:10.1175/MWR-D-13-00101.1.
- , D. W. Burgess, E. R. Mansell, and L. J. Wicker, 2015a: Bulk hook echo raindrop sizes retrieved using mobile, polarimetric Doppler radar observations. *J. Appl. Meteor. Climatol.*, **54**, 423–450, doi:10.1175/JAMC-D-14-0171.1.
- , P. S. Skinner, L. J. Wicker, and H. B. Bluestein, 2015b: Documenting a rare tornado merger observed in the 24 May 2011 El Reno–Piedmont, Oklahoma, supercell. *Mon. Wea. Rev.*, **143**, 3025–3043, doi:10.1175/MWR-D-14-00349.1.
- Fujita, T. T., 1981: Tornadoes and downbursts in the context of generalized planetary scales. *J. Atmos. Sci.*, **38**, 1511–1534, doi:10.1175/1520-0469(1981)038<1511:TADITC>2.0.CO;2.
- Heinselman, P. L., D. L. Prieegnitz, K. L. Manross, T. M. Smith, and R. W. Adams, 2008: Rapid sampling of severe storms by the national weather radar testbed phased array radar. *Wea. Forecasting*, **23**, 808–824, doi:10.1175/2008WAF2007071.1.
- Houser, J. B., H. B. Bluestein, and J. C. Snyder, 2015: Rapid-scan, polarimetric, Doppler-radar observations of tornadogenesis and tornado dissipation in a tornadic supercell: The “El Reno, Oklahoma” storm of 24 May 2011. *Mon. Wea. Rev.*, **143**, 2685–2710, doi:10.1175/MWR-D-14-00253.1.
- , —, and —, 2016: A finescale radar examination of the tornadic debris signature and weak-echo reflectivity band associated with a large, violent

- tornado. *Mon. Wea. Rev.*, **144**, 4101–4130, doi:10.1175/MWR-D-15-0408.1.
- Isom, B., and Coauthors, 2013: The atmospheric imaging radar: Simultaneous volumetric observations using a phased array weather radar. *J. Atmos. Oceanic Technol.*, **30**, 655–675, doi:10.1175/JTECH-D-12-00063.1.
- Jain, A., 1989: *Fundamentals of Digital Image Processing*. Prentice-Hall, 569 pp.
- Kosiba, K. A., and J. Wurman, 2013: The three-dimensional structure and evolution of a tornado boundary layer. *Wea. Forecasting*, **28**, 1552–1561, doi:10.1175/WAF-D-13-00070.1.
- , —, Y. Richardson, P. Markowski, P. Robinson, and J. Marquis, 2013: Genesis of the Goshen County, Wyoming, tornado on 5 June 2009 during VORTEX2. *Mon. Wea. Rev.*, **141**, 1157–1181, doi:10.1175/MWR-D-12-00056.1.
- Kurdzo, J. M., B. L. Cheong, R. D. Palmer, G. Zhang, and J. Meier, 2014: A pulse compression waveform for improved-sensitivity weather radar observations. *J. Atmos. Oceanic Technol.*, **31**, 2713–2731, doi:10.1175/JTECH-D-13-00021.1.
- , D. J. Bodine, B. L. Cheong, and R. D. Palmer, 2015: High-temporal resolution polarimetric X-band Doppler radar observations of the 20 May 2013 Moore, Oklahoma, tornado. *Mon. Wea. Rev.*, **143**, 2711–2735, doi:10.1175/MWR-D-14-00357.1.
- Lee, B. D., C. A. Finley, and C. D. Karstens, 2012a: The Bowdle, South Dakota, cyclic tornadic supercell of 22 May 2010: Surface analysis of rear-flank downdraft evolution and multiple internal surges. *Mon. Wea. Rev.*, **140**, 3419–3441, doi:10.1175/MWR-D-11-00351.1.
- Lee, P., A. P. Jayasumana, H. Dilum Bandara, S. Lim, and V. Chandrasekar, 2012b: A peer-to-peer collaboration framework for multi-sensor data fusion. *J. Network Comput. Appl.*, **35**, 1052–1066, doi:10.1016/j.jnca.2011.12.005.
- Lemon, L. R., and C. A. Doswell, 1979: Severe thunderstorm evolution and mesocyclone structure as related to tornadogenesis. *Mon. Wea. Rev.*, **107**, 1184–1197, doi:10.1175/1520-0493(1979)107<1184:STEAMS>2.0.CO;2.
- Lewellen, D. C., B. Gong, and W. S. Lewellen, 2008: Effects of finescale debris on near-surface tornado dynamics. *J. Atmos. Sci.*, **65**, 3247–3262, doi:10.1175/2008JAS2686.1.
- Lewellen, W. S., D. C. Lewellen, and R. I. Sykes, 1997: Large-eddy simulation of a tornado's interaction with the surface. *J. Atmos. Sci.*, **54**, 581–605, doi:10.1175/1520-0469(1997)054<0581:LESOAT>2.0.CO;2.
- Markowski, P. M., 2002: Hook echoes and rear-flank downdrafts: A review. *Mon. Wea. Rev.*, **130**, 852–876, doi:10.1175/1520-0493(2002)130<0852:HEARFD>2.0.CO;2.
- , and Y. P. Richardson, 2014: What we know and don't know about tornado formation. *Phys. Today*, **67**, 26–31, doi:10.1063/PT.3.2514.
- , J. M. Straka, and E. N. Rasmussen, 2002: Direct surface thermodynamic observations within the rear-flank downdrafts of nontornadic and tornadic supercells. *Mon. Wea. Rev.*, **130**, 1692–1721, doi:10.1175/1520-0493(2002)130<1692:DSTOWT>2.0.CO;2.
- , and Coauthors, 2012a: The pretornadic phase of the Goshen County, Wyoming, supercell of 5 June 2009 intercepted by VORTEX2. Part I: Evolution of kinematic and surface thermodynamic fields. *Mon. Wea. Rev.*, **140**, 2887–2915, doi:10.1175/MWR-D-11-00336.1.
- , and Coauthors, 2012b: The pretornadic phase of the Goshen County, Wyoming, supercell of 5 June 2009 intercepted by VORTEX2. Part II: Intensification of low-level rotation. *Mon. Wea. Rev.*, **140**, 2916–2938, doi:10.1175/MWR-D-11-00337.1.
- Marquis, J., Y. Richardson, J. Wurman, and P. Markowski, 2008: Single- and dual-Doppler analysis of a tornadic vortex and surrounding storm-scale flow in the Crowell, Texas, supercell of 30 April 2000. *Mon. Wea. Rev.*, **136**, 5017–5043, doi:10.1175/2008MWR2442.1.
- , —, P. Markowski, D. Dowell, and J. Wurman, 2012: Tornado maintenance investigated with high-resolution dual-Doppler and EnKF analysis. *Mon. Wea. Rev.*, **140**, 3–27, doi:10.1175/MWR-D-11-00025.1.
- , —, —, —, —, K. Kosiba, P. Robinson, and G. Romine, 2014: An investigation of the Goshen County, Wyoming, tornadic supercell of 5 June 2009 using EnKF assimilation of mobile mesonet and radar observations collected during VORTEX2. Part I: Experiment design and verification of the EnKF analyses. *Mon. Wea. Rev.*, **142**, 530–554, doi:10.1175/MWR-D-13-00007.1.
- McLaughlin, D., and Coauthors, 2009: Short-wavelength technology and the potential for distributed networks of small radar systems. *Bull. Amer. Meteor. Soc.*, **90**, 1797–1817, doi:10.1175/2009BAMS2507.1.
- Mead, J. B., G. Hopcraft, S. J. Frasier, B. D. Pollard, C. D. Cherry, D. H. Schaubert, and R. E. McIntosh, 1998: A volume-imaging radar wind profiler for atmospheric boundary layer turbulence studies. *J. Atmos. Oceanic Technol.*, **15**, 849–859, doi:10.1175/1520-0426(1998)015<0849:AVIRWP>2.0.CO;2.

- Otsuka, S., and Coauthors, 2016: Precipitation nowcasting with three-dimensional space–time extrapolation of dense and frequent phased-array weather radar observations. *Wea. Forecasting*, **31**, 329–340, doi:10.1175/WAF-D-15-0063.1.
- Palmer, R. D., B. L. Cheong, M. W. Hoffman, S. J. Frasier, and F. J. López-Dekker, 2005: Observations of the small-scale variability of precipitation using an imaging radar. *J. Atmos. Oceanic Technol.*, **22**, 1122–1137, doi:10.1175/JTECH1775.1.
- Park, H. S., A. V. Ryzhkov, D. S. Zrnić, and K.-E. Kim, 2009: The hydrometeor classification algorithm for the polarimetric WSR-88D: Description and application to an MCS. *Wea. Forecasting*, **24**, 730–748, doi:10.1175/2008WAF2222205.1.
- Pazmany, A. L., J. B. Mead, H. B. Bluestein, J. C. Snyder, and J. B. Houser, 2013: A mobile rapid-scanning X-band polarimetric (RaXPoL) Doppler radar system. *J. Atmos. Oceanic Technol.*, **30**, 1398–1413, doi:10.1175/JTECH-D-12-00166.1.
- Ryzhkov, A. V., T. J. Schurr, D. W. Burgess, and D. Zrnić, 2005: Polarimetric tornado detection. *J. Appl. Meteor. Climatol.*, **44**, 557–570, doi:10.1175/JAM2235.1.
- Schenkman, A. D., M. Xue, and D. T. Dawson II, 2016: The cause of internal outflow surges in a high-resolution simulation of the 8 May 2003 Oklahoma City tornadic supercell. *J. Atmos. Sci.*, **73**, 353–370, doi:10.1175/JAS-D-15-0112.1.
- Schultz, C. J., and Coauthors, 2012: Dual-polarization tornadic debris signatures Part I: Examples and utility in an operational setting. *Electron. J. Oper. Meteor.*, **13** (9), 120–137.
- Skinner, P. S., C. C. Weiss, M. M. French, H. B. Bluestein, P. M. Markowski, and Y. P. Richardson, 2014: VORTEX2 observations of a low-level mesocyclone with multiple internal rear-flank downdraft momentum surges in the 18 May 2010, Dumas, Texas supercell. *Mon. Wea. Rev.*, **142**, 2935–2960, doi:10.1175/MWR-D-13-00240.1.
- , —, L. J. Wicker, C. K. Potvin, and D. C. Dowell, 2015: Forcing mechanisms for an internal rear-flank downdraft momentum surge in the 18 May 2010 Dumas, Texas supercell. *Mon. Wea. Rev.*, **143**, 4305–4330, doi:10.1175/MWR-D-15-0164.1.
- Skolnik, M., 2002: *Introduction to Radar Systems*. 3rd ed., McGraw-Hill, 772 pp.
- Snyder, J. C., and H. B. Bluestein, 2014: Some considerations for the use of high-resolution mobile radar data in tornado intensity determination. *Wea. Forecasting*, **29**, 799–827, doi:10.1175/WAF-D-14-00026.1.
- , —, V. Venkatesh, and S. J. Frasier, 2013: Observations of polarimetric signatures in supercells by an X-band mobile Doppler radar. *Mon. Wea. Rev.*, **141**, 3–29, doi:10.1175/MWR-D-12-00068.1.
- Straka, J. M., D. S. Zrnić, and A. V. Ryzhkov, 2000: Bulk hydrometeor classification and quantification using polarimetric radar data: Synthesis of relations. *J. Appl. Meteor. Climatol.*, **39**, 1341–1372, doi:10.1175/1520-0450(2000)039<1341:BHCAQU>2.0.CO;2.
- Tanamachi, R. L., H. B. Bluestein, J. B. Houser, S. J. Frasier, and K. M. Hardwick, 2012: Mobile, X-band, polarimetric Doppler radar observations of the 4 May 2007 Greensburg, Kansas, tornadic supercell. *Mon. Wea. Rev.*, **140**, 2103–2125, doi:10.1175/MWR-D-11-00142.1.
- , —, M. Xue, W.-C. Lee, K. A. Orzel, S. J. Frasier, and R. M. Wakimoto, 2013: Near-surface vortex structure in a tornado and in a sub-tornado-strength convective-storm vortex observed by a mobile, W-band radar during VORTEX2. *Mon. Wea. Rev.*, **141**, 3661–3690, doi:10.1175/MWR-D-12-00331.1.
- Ushio, T., and Coauthors, 2014: Development and observation of the phased array radar at X band. *2014 XXXIth URSI General Assembly and Scientific Symposium (URSI GASS)*, IEEE, 1–4, doi:10.1109/URSIGASS.2014.6929643.
- Van Den Broeke, M. S., 2015: Polarimetric tornadic debris signature variability and debris fallout signatures. *J. Appl. Meteor. Climatol.*, **54**, 2389–2405, doi:10.1175/JAMC-D-15-0077.1.
- Wakimoto, R. M., N. T. Atkins, and J. Wurman, 2011: The LaGrange tornado during VORTEX2. Part I: Photogrammetric analysis of the tornado combined with single-Doppler radar data. *Mon. Wea. Rev.*, **139**, 2233–2258, doi:10.1175/2010MWR3568.1.
- , P. Stauffer, W.-C. Lee, N. T. Atkins, and J. Wurman, 2012: Finescale structure of the LaGrange, Wyoming, tornado during VORTEX2: GBVTD and photogrammetric analyses. *Mon. Wea. Rev.*, **140**, 3397–3418, doi:10.1175/MWR-D-12-00036.1.
- , N. T. Atkins, K. M. Butler, H. B. Bluestein, K. Thiem, J. Snyder, and J. Houser, 2015: Photogrammetric analysis of the 2013 El Reno tornado combined with mobile X-band polarimetric radar data. *Mon. Wea. Rev.*, **143**, 2657–2683, doi:10.1175/MWR-D-15-0034.1.
- , and Coauthors, 2016: Aerial damage survey of the 2013 El Reno tornado combined with mobile radar data. *Mon. Wea. Rev.*, **144**, 1749–1776, doi:10.1175/MWR-D-15-0367.1.
- Weber, M. E., J. Y. N. Cho, J. S. Herd, J. M. Flavin, W. E. Benner, and G. S. Torok, 2007: The next-generation multimission U.S. surveillance radar network. *Bull. Amer. Meteor. Soc.*, **88**, 1739–1751, doi:10.1175/BAMS-88-11-1739.
- Wurman, J., 2002: The multiple-vortex structure of a tornado. *Wea. Forecasting*, **17**, 473–505, doi:10.1175/1520-0434(2002)017<0473:TMVSOA>2.0.CO;2.

- , and S. Gill, 2000: Finescale radar observations of the Dimmitt, Texas (2 June 1995), tornado. *Mon. Wea. Rev.*, **128**, 2135–2164, doi:10.1175/1520-0493(2000)128<2135:FROOTD>2.0.CO;2.
- , and M. Randall, 2001: An inexpensive, mobile, rapid-scan radar. *30th Int. Conf. on Radar Meteorology*, Munich, Germany, Amer. Meteor. Soc., P3.4. [Available online at https://ams.confex.com/ams/30radar/techprogram/paper_21577.htm.]
- , and T. Samaras, 2004: Comparison of in situ pressure and DOW Doppler winds in a tornado and RHI vertical slices through 4 tornadoes during 1996–2004. *22nd Conf. on Severe Local Storms*, Hyannis, MA, Amer. Meteor. Soc., 15.4. [Available online at https://ams.confex.com/ams/11aram22sls/techprogram/paper_82352.htm.]
- , and C. R. Alexander, 2005: The 30 May 1998 Spencer, South Dakota, storm. Part II: Comparison of observed damage and radar-derived winds in the tornadoes. *Mon. Wea. Rev.*, **133**, 97–119, doi:10.1175/MWR-2856.1.
- , and K. Kosiba, 2013: Finescale radar observations of tornado and mesocyclone structures. *Wea. Forecasting*, **28**, 1157–1174, doi:10.1175/WAF-D-12-00127.1.
- , J. M. Straka, and E. N. Rasmussen, 1996: Fine-scale Doppler radar observations of tornadoes. *Science*, **272**, 1774–1777, doi:10.1126/science.272.5269.1774.
- , Y. Richardson, C. Alexander, S. Weygandt, and P. F. Zhang, 2007a: Dual-Doppler analysis of winds and vorticity budget terms near a tornado. *Mon. Wea. Rev.*, **135**, 2392–2405, doi:10.1175/MWR3404.1.
- , —, —, —, and —, 2007b: Dual-Doppler and single-Doppler analysis of a tornadic storm undergoing mergers and repeated tornadogenesis. *Mon. Wea. Rev.*, **135**, 736–758, doi:10.1175/MWR3276.1.
- , K. Kosiba, P. Markowski, Y. Richardson, D. Dowell, and P. Robinson, 2010: Finescale single- and dual-Doppler analysis of tornado intensification, maintenance, and dissipation in the Orleans, Nebraska, supercell. *Mon. Wea. Rev.*, **138**, 4439–4455, doi:10.1175/2010MWR3330.1.
- , —, and P. Robinson, 2013: In situ, Doppler radar, and video observations of the interior structure of a tornado and the wind–damage relationship. *Bull. Amer. Meteor. Soc.*, **94**, 835–846, doi:10.1175/BAMS-D-12-00114.1.
- , —, —, and T. Marshall, 2014: The role of multiple-vortex tornado structure in causing storm researcher fatalities. *Bull. Amer. Meteor. Soc.*, **95**, 31–45, doi:10.1175/BAMS-D-13-00221.1.
- Zrnić, D. S., and Coauthors, 2007: Agile-beam phased array radar for weather observations. *Bull. Amer. Meteor. Soc.*, **88**, 1753–1766, doi:10.1175/BAMS-88-11-1753.

AMS titles now available as eBooks at **springer.com**

AMS BOOKS

RESEARCH APPLICATIONS HISTORY

www.ametsoc.org/amsbookstore



Scan to see
AMS eBook titles
at springer.com



AMERICAN METEOROLOGICAL SOCIETY